PCCP

Accepted Manuscript

ROYAL SOCIETY OF CHEMISTRY

www.rsc.org/pccp

Understanding the synergistic effect of WO_3-$BiVO_4$ heterostructures by impedance spectroscopy

Xinjian Shi,[1,†] Isaac Herraiz-Cardona,[2,†] Luca Bertoluzzi,[2] Pilar Lopez-Varo,[3] Juan Bisquert,[2,4] Jong Hyeok Park,[5,*] Sixto Gimenez[2,*]

[1]*Department of Mechanical Engineering, Stanford University, Stanford, California 94305, United States*

[2]*Institute of Advanced Materials (INAM), Universitat Jaume I, 12071 Castelló, Spain*

[3]*Departamento de Electrónica y Tecnología de Computadores, CITIC-UGR, Universidad de Granada, 18071 Granada, Spain*

[4]*Department of Chemistry, Faculty of Science, King Abdulaziz University, Jeddah 21589, Saudi Arabia*

[5]*Department of Chemical and Biomolecular Engineering, Yonsei University, 50 Yonsei-ro, Seodaemun-gu, Seoul 120-749, Republic of Korea*

Email: lutts@skku.edu, sjulia@uji.es

26 February 2016

Abstract

WO_3-$BiVO_4$ n-n heterostructures have demonstrated remarkable performance for photoelectrochemical water splitting due to the synergistic effect between the individual components. Although the enhanced functional capabilities of this system have been widely reported, in-depth mechanistic studies explaining the carrier dynamics of this heterostructure are limited. The main goal is providing rational design strategies for further optimization as well as to extend these strategies to different candidate systems for solar fuel production. In the present study, we perform a systematic optoelectronic and photoelectrochemical characterization to understand the carrier dynamics of the system and develop a simple physical model to highlight the importance of the selective contacts to minimize bulk recombination in this heterostructure. Our results collectively indicate that while $BiVO_4$ is responsible for the enhanced optical properties, WO_3 controls the transport properties of the heterostructured WO_3-$BiVO_4$ system, leading to reduced bulk recombination.

Keywords: photoelectrochemical cells, solar fuels, water splitting, heterojunction, synergistic effect

Introduction

Photoelectrochemical water splitting with semiconductor materials has emerged as one of the most promising approaches to produce hydrogen (H_2) from renewable resources as sunlight and water. This produced hydrogen can be employed as an energy vector in different energy converting schemes, but also as a valuable feedstock for the chemical industry. The current solar-to-hydrogen efficiencies (STH) achieved in champion devices are still not competitive for technological deployment, and intensive research activity is taking place in material development and device engineering in order to narrow the gap between achieved and targeted performances. Moreover, recent techno-economic analysis predict that the future implementation of this technology will depend on the feasibility of efficient and durable devices targeting 2-4 $ per kg of dispensed H_2.[1] Consequently, low-cost materials and synthetic strategies are at the forefront of the research to achieve this goal. Metal oxides like TiO_2,[2] ZnO,[3] WO_3,[4] $BiVO_4$,[5]or Fe_2O_3,[6] have been thoroughly investigated as candidate photoanodes since these materials are abundant in the earth crust and exhibit excellent stability for water oxidation. However, the low photocurrents constitute a serious obstacle for competitive efficiencies. In some cases, this is derived from the large bandgaps of metal oxides like TiO_2 or ZnO_2.[7, 8] In other cases, poor electronic properties (Fe_2O_3, $BiVO_4$) are mainly responsible for the low performance. As an example, champion photocurrent for Fe_2O_3 at 1.23 V vs RHE is close to 4 mA/cm^2,[9, 10] significantly below its theoretical photocurrent (12 mA/cm^2) highlighting the excessive recombination losses for this material. On the other hand, important advances have been achieved to bring the photovoltage of Fe_2O_3 in contact with water to its theoretical maximum (0.8 V), by restoring surface defects of the material and enhancing the water oxidation kinetics by

the use of efficient catalysts.[11] On the other hand, record photocurrent of 5 mA/cm^2 at 1.23 V vs RHE has been obtained by the "defect-tolerant" bismuth vanadate, $BiVO_4$, closer to its theoretical maximum (7.5 mA/cm^2) by nanostructuring strategies coupled to efficient water oxidation catalysts.[12] The introduction of a gradient dopant concentration in the metal oxide film creating a distributed n^+–n homojunction has also demonstrated to be particularly useful to overcome the high recombination losses of $BiVO_4$, showing a remarkable increase of the carrier separation efficiency from ~38% to more than 60% at 1.23 V vs. RHE.[13] Engineered heterostructures can also overcome this low charge separation efficiency of $BiVO_4$, and WO_3-$BiVO_4$ is a nice example of composite structure, synergistically combining merits of the two semiconductors, *i.e.* excellent charge transport characteristics of WO_3 and good light absorption efficiency of $BiVO_4$.[14-19] Record water splitting photocurrents of 6.72 mA/cm^2 under 1 sun illumination at 1.23 V vs RHE corresponding to ~90% of the theoretically possible value for $BiVO_4$ have been recently reported together with a self-biased operation of the photoanode in tandem with a photovoltaic device providing 8.1% STH efficiency.[19] The enhanced performance of these heterostructures has been generally attributed to the improved charge separation properties of the $BiVO_4$ absorber, rather than to the optical enhancement obtained from the combination of both semiconductors.[15, 16] In addition, one-dimensional structures also benefit from vectorial carrier transport (reduced bulk recombination) as well as strong scattering effects (enhanced light harvesting), which collectively lead to enhanced conversion efficiencies.[16, 19, 20] Despite the remarkable progress in terms of photoelectrochemical behavior of WO_3-$BiVO_4$ heterojunctions achieved during the last years, the knowledge on the carrier dynamics of this system is limited. In the present study, we provide a detailed evaluation of the

photoelectrochemical behavior of these heterostructures, based on the combined dynamic characterization and modeling of the basic processes leading to water oxidation. Aiming at a simple treatment of the problem, we have focused on the characterization of the individual materials (both WO_3 and $BiVO_4$) as a reference for the heterostructured WO_3-$BiVO_4$ system. Additionally, we have addressed nanoparticulated systems, morphologically less complex than one-dimensional structures in terms of modeling, although higher performance has been generally reported for the latter structures.[16, 19, 20]

Methods

Materials preparation and experimental process

Fabrication of WO_3 host layer: In order to prepare a WO_3 host layer porous for $BiVO_4$ guest material penetration and precise control of the particle size, the surfactant-assisted synthesis was used. First, 0.9 g of tungsten powder was slowly dissolved in 5 ml H_2O_2 (35%, Junsei), and subsequently stirred for 6 h. Second, 10 ml 2-propanol ($(CH_3)_2CHOH$ Junsei) was further added into the precursor solution with continuous stirring for one more day. Third, 8 ml of polyethylene glycol (PEG, Aldrich) was added as the final step for the preparation of the precursor solution to control the morphology. On the other hand, fluorine-doped tin oxide (FTO, TEC-8, Pilkilton) glasses were properly conditioned for the deposition of the precursor solution. By using the mixture of ethanol and acetone (1:1 by vol%), FTO substrates were cleaned for 10 min with sonication, and then the glasses were put into H_2SO_4/H_2O_2 mixed solution for another 10 min, to make its surface hydrophilic for the subsequent drop casting step. Note that the FTO substrates should be placed on an optical table with an extremely flat surface

during the drop casting process. Afterwards, the sample was dried at room temperature for approximately 20 min for the even distribution of the solution on top of the FTO substrate. Finally, the samples were annealed at 550°C for 2 h, with extremely slow temperature increase (2°C/min). Since the main objective of the present study relates to the evaluation of operating physico-chemical mechanisms rather than to obtain samples with optimized performance, only one cycle of the fabrication process was conducted. In this way, the evaluation of carrier dynamics on the WO_3 and $BiVO_4$ specimens is expected to be simpler, since higher sample reproducibility is envisaged.

The addition of $BiVO_4$ guest material: The $BiVO_4$ precursor solution was made from the bismuth nitrate hexahydrate ($BiN_3O_9{\cdot}5H_2O$, 99.99% Aldrich), the Bi source, and vanadyl acetylacetonate ($C_{10}H_{14}O_5V$,98% Aldrich), the V source, which were added to an acetylacetone ($C_5H_8O_2$, Fluka) and acetic acid (CH_3COOH, 99.70%, DAE) mixed solution, with volume amount 25:3. Then the precursor solution was put in an oven with 60°C for 10 min to dissolve the powders and obtain the dark green solution. Usually it is better to use the precursor made by this method within one day after it is prepared, to avoid the sedimentation. The final molar concentration of Bi is around 36 mM which is approximately equal to the molar concentration of V. Then, in a dry and well-ventilated environment, 40 μl of the as-prepared $BiVO_4$ precursor solution were slowly dropped on the porous WO_3 host layer and the sample was kept there for 30 min for solution penetration into the WO_3 layer. Finally, an annealing process was carried out under 500^{o}C for 2 h in a furnace.

Characterization techniques.

UV-vis spectra were recorded by using a UV–Vis spectrophotometer (UV-2401 PC, Shimadzu). Morphology analysis of the samples was carried out using field-emission

scanning electron microscopy (FESEM, JEOLJSM-7000F, Japan) and transmission electron microscopy (TEM, JEOL JEM-2100F, Japan). Current density voltage (*j-V*) and electrochemical impedance spectroscopy (EIS) measurements were carried out using a FRA equipped PGSTAT-30 potentiostat from Autolab. A three-electrode configuration was used, where a Pt foil and an Ag/AgCl (3 M KCl) electrode were used as counter-electrode and as reference electrode, respectively. The electrolyte was a 0.5 M Na_2SO_4 aqueous solution (in pH 7 phosphate buffer). Some photoelectrochemical tests were carried out in the presence of an efficient hole scavenger (0.35 M Na_2SO_3). The electrodes (geometrical area ca. 0.9 cm^2) were illuminated using a 300 W Xe lamp, where the light intensity was adjusted with a thermopile to 100 mW cm^{-2}. EIS measurements were carried out by applying a 20 mV AC signal and scanning in a frequency range between 100 kHz and 50 mHz, at different applied bias. The numerical fitting of the impedance data was carried out using the Zview software (Scribner Associates).

Results and Discussion

In order to assess the photoelectrochemical behavior of water oxidation for both reference materials and the heterostructured system, the *j-V* curves of $BiVO_4$, WO_3 and the WO_3-$BiVO_4$ photoelectrodes in the dark and under illumination at 100 mW·cm^{-2} are shown in **Figure 1a**.The lowest photocurrent is measured for $BiVO_4$, as a result of the high recombination losses of this material. Higher photocurrents are measured for WO_3 in spite of its larger bandgap, due to its higher conductivity.[18] The sudden rise observed above 2.0 V *vs.* RHE is attributed to charge transfer through the FTO substrate to the solution, due to the nanoparticulated morphology of the film. Significantly higher

photocurrents are measured for the heterostructured material, (six-fold enhancement at the photocurrent plateau) which cannot be solely attributed to the enhanced light harvesting efficiency of the composite (**Figure S1**), in good agreement with previous studies.[16] Indeed, from the absorption spectra of both WO_3 and $BiVO_4$ films, the estimated optical bandgaps were extracted by using the Tauc plots for direct bandgap transition (shown in **Figure S2**). The obtained values ($E_{g\ WO3}$= 2.92 eV, $E_{g\ BiVO4}$= 2.40 eV) are in excellent correspondence with those reported in literature.[21]

Figure 1b shows the *j-V* curves when a hole scavenger (0.35 M Na_2SO_3) is present in the solution. Enhanced photocurrent is again observed for the heterostructured material indicating that the synergistic effect is not related to surface catalysis. Indeed, the higher photocurrent for $BiVO_4$ in this condition, compared to WO_3, highlights the sluggish charge transfer to the solution of $BiVO_4$ for water oxidation. From the values of optical absorbance of the materials (**Figure S1**) and the photocurrents with and without hole scavenger (**Figure 1**), the maximum photocurrent (j_{abs}), the charge separation efficiency (η_{cs}) and the charge injection efficiency (η_{cat}) were calculated according to reference [22]. The obtained results are compiled as **Figure S3** and **Table S1** and clearly illustrate the poor charge injection efficiency of $BiVO_4$. On the other hand, the charge separation efficiency of the WO_3-$BiVO_4$ heterostructure is significantly improved compared to both individual materials, in good agreement with previous studies.[16]

Impedance spectroscopy measurements were carried out in the dark and under illumination in order to further assess the electronic processes taking place in the different materials leading to water oxidation. The typical complex plane plots obtained for all samples are displayed in **Figure S4.** Two main features should be highlighted from such spectra. Firstly, at low applied bias, the Nyquist plots of the photoanodes

containing WO_3 nanoparticles (NP) systematically exhibited a high frequency deformed arc, resulting from the coupling between the transmission line, characteristic of electron diffusion, and the capacitance of the FTO.[23, 24] Secondly, the spectra obtained for pure $BiVO_4$ photoanodes did not show any feature related to electron transport.

In order to fit the EIS data, we employed the equivalent circuits showed in **Figure 2**. In **Figure 2**, R_s accounts for the series resistance of the electrochemical cell, including the contribution of the contacts, connection wires, etc., R_{FTO} conveys the information of the charge transfer resistance at the FTO/NP interface, C_{FTO} models the capacitance of the FTO/solution interface and *TL* is an extended element, accounting for the carrier transport ($R_t = r_t \cdot L$) through the mesoporous film coupled to charge transfer to the solution (R_{ct}), the capacitance at the semiconductor nanostructure including the NP/solution interface (C_0 or C_{film}). Note that the latter capacitance includes the effect of a variation of the electron concentration in the conduction band as well as the variation of the electric field in the depletion region.[25]

The transport resistance (R_t) provides information about the film conductivity (σ) through the expression:

$$\sigma = \frac{L}{R_t A(1-p)} \quad (1)$$

Where L is the film thickness, A is the geometrical area of the specimens and p is the porosity of the film (p = 0.45 and 0.40 for WO_3 and WO_3-$BiVO_4$, respectively, taken as a first approximation from cross sectional microscopy and the morphological information shown in **Figure S5**). Since transport limitations are not visible in compact $BiVO_4$ samples, the electrical equivalent circuit is simplified to the parallel association of C_{film} and R_{ct}, see **Figure 2c**. Note that through EIS one only has access to the majority

carrier concentration (electrons).[25] Therefore, the extracted conductivity is solely associated to electrons, and increases along with electron injection, i.e. when sweeping voltage to the cathodic direction or under illumination.

Both in the dark and under illumination, the capacitance of $BiVO_4$ is practically constant around 10 $\mu F \cdot cm^{-2}$ (**Figures 3b** and **e**), which is a typical value for a double layer capacitance. A capacitive peak at 0.8V *vs.* RHE is probably related to the change in vanadium oxidation state V^{+4}/V^{+5}.[26, 27] Conversely, the capacitances of WO_3 and WO_3-$BiVO_4$ show identical exponential behavior with applied voltage in the dark, clearly indicating that WO_3 controls the capacitance of the heterostructured material. This is consistent with the few nanometers thickness of $BiVO_4$ in the heterostructured film as clearly observed in the HR-TEM micrograph showed in **Figure S5e**.

The exponential dependence of capacitance with applied voltage is characteristic of the chemical capacitance, and monitors the exponential density of states below the conduction band. This behavior has been systematically observed for semiconductor materials like TiO_2.[28] Under illumination, the capacitance of the heterostructured material is higher compared to the WO_3 host. This effect is probably related to the enhanced electron density at the WO_3 material, due to the injection of photogenerated charges from the $BiVO_4$ guest.

Furthermore, the conductivity data display two interesting features. On the first hand, the conductivities of WO_3 and WO_3-$BiVO_4$ electrodes in the dark (**Figure 3a**) are identical, also indicating that the transport properties of the heterostructure are dominated by the WO_3 host, which drives the electronic charge toward the contact. Under illumination, the conductivity of the heterostructured material is higher compared to WO_3 (**Figure 3d**), in good agreement with the increased electron density. On the

other hand, transport limitations are observed in WO_3 but not in the $BiVO_4$photoanode. Such observation may appear to be in stark contrast with previous reports from the literature.[16] However it must be emphasized that diffusion limitation in WO_3 is due to the poor carrier photogeneration, and its resulting low conductivity, unlike in $BiVO_4$. In the WO_3-$BiVO_4$ heterostructure under illumination, transport properties are significantly improved due to the injection of photogenerated electrons from the $BiVO_4$ absorber to the WO_3 nanoparticle network. This observation corroborates the increase in capacitance for the WO_3-$BiVO_4$ heterostructure under illumination.

Finally, **Figures 3f** and **3c** show the evolution with voltage of the dc resistance, R_{dc}, (also named total resistance), which contains all the faradic contributions to the current density. The dc resistance allows eliminating unnecessary information present in a *j-V* curve, which blurs the analysis of the recombination processes. In fact the dc resistance permits to have a clear and general picture of the voltage dependent processes, (i.e. recombination), by eliminating the contributions from constant sources, which do not vary with voltage, (carrier photogeneration). Therefore, it is a very convenient way to compare recombination processes for different devices. In particular, the analysis of this resistance can give valuable information on the type of recombination which limits device performance, as explained later on. Under illumination (**Figure 3f**), R_{dc} systematically shows a valley, which takes place simultaneously with the inflection point of the *j-V* curve. Consequently, this resistance is basically reflected in the derivative behavior of the *j-V* curve, and we can define it as $R_{dc} = (\partial \bar{j}/\partial V)^{-1}$.

So far, our EIS analysis has revealed enhanced photoelectrochemical performances for the $BiVO_4$-WO_3 heterostructure for water oxidation due to photogenerated carrier injection from $BiVO_4$ to WO_3. Yet, it is not clear at this point whether charge transport

is enhanced by reduction of the recombination kinetics or carrier extraction at the contact. In order to more accurately discriminate the mechanisms leading to device operation for the three tested materials, we considered the physical model depicted in **Figure 4**. For the sake of simplicity, we consider the n-n WO_3-$BiVO_4$ heterostructure as a single n type semiconductor with a rectifying contact for the minority carriers (holes) at the semiconductor/electrolyte interface and an ohmic contact for the majority carriers at the metal/semiconductor interface. The difference between WO_3-$BiVO_4$ heterostructure and one semiconductor alone, in our model, is the different amount of recombination.

Indeed, the use of the heterostructured $BiVO_4$-WO_3 architecture can affect the photoelectrochemical performance in two different ways. First, bulk recombination of photogenerated carriers (generated at a rate G) can be modified, which is taken into account in our model via the bulk factor, B, which controls the recombination rate, U_r, defined as:

$$U_r = B\left(\bar{n}\bar{p} - n_0 p_0\right) \quad (2)$$

Where $\bar{n}$ and $\bar{p}$ are the steady state concentrations of electrons and holes, and the subscript 0 indicates equilibrium concentrations. It must be remarked that higher values of the bulk recombination kinetic factor produce higher recombination rates. In addition, it should be noted that bulk recombination can also be modulated by the carrier mobility (or diffusion coefficient). Indeed, lower carrier mobility induces higher bulk recombination. However, in steady state measurements, it is a priori impossible to distinguish between low carrier mobility and higher recombination kinetics. For this reason, in our simulations we fixed the carrier mobility for all samples and we varied the kinetics of recombination via the parameter B.

Second, electron extraction at the electron selective contact may be modified. Such feature is taken into account in our model via the electron surface recombination velocity, S_n, which regulates the current at the electron selective contact:

$$\bar{j} = qS_n(\bar{n}(L=0) - n_0) \quad (3)$$

It should be remarked that the parameter S_n is commonly termed the surface recombination. However, in contrast to the bulk recombination factor, B, larger values of S_n induce larger values of the current. Therefore, this type of recombination (also termed charge transfer) is beneficial in term of photo-electrochemical performance.

Similarly, sluggish hole transfer at the semiconductor/electrolyte interface is tuned by the hole surface recombination velocity, S_p, which governs the current at the semiconductor/electrolyte interface:

$$\bar{j} = qS_p(\bar{p}(L) - p_0) \quad (4)$$

At this point we should emphasize that in steady state measurements, one cannot discriminate between poorer extraction kinetics of either electron or hole. In other words, it is not feasible to tell whether S_p or S_n affects carrier extraction at the contacts. For this reason we assumed S_p to be identical for all the materials used in our simulations and we varied only the parameter S_n.This statement is consistent with the results showed in **Figure 1b** performed in an electrolyte containing a hole scavenger and by the EIS experiments with this electrolyte solution, which are summarized in **Figure S6**.

In order to identify which of these two recombination processes is dominating the photo-electrochemical performances of WO_3, $BiVO_4$ and WO_3-$BiVO_4$ presented in **Figure 1** and **Figure 3**, we simulated the *j-V* characteristic and the dc resistance,

previously defined. The continuity equations were solved along with Poisson equation, which controls the electric field within the device. More details on the equations used for our modeling are given in SI, "Model equations" part.

In **Figure 5a**, we show how bulk and surface recombination affect the *j-V* characteristics. As expected, the current is zero at cathodic bias ($< -0.5\ V$), close to the flat band potential, due to the sluggish electron extraction at the semiconductor/metal contact. When sweeping to anodic potentials, the height of the Schottky barrier at the semiconductor/solution interface increases. As a consequence, recombination drops and the current rises until reaching saturation once the recombination of photo-generated holes completely vanishes. However, as can be observed from **Figure 5a**, bulk and surface recombination mainly affect the onset voltage in our simulations although the effects of both processes cannot be distinguished.

In **Figure 5b**, we note how the resistance of the system reaches a minimum, the so called valley observed in **Figure 3f**, which corresponds to the inflection point in the *j-V* curve. It should also be remarked that for perfect selective contacts, with high values of S_n and S_p, there is no more plateau at low bias and no minimum is observed in the resistance (**Figure S7**). Consequently the presence of a minimum in the total resistance indicates sluggish carrier extraction at one or both contacts. The effect of increasing the surface recombination, via the parameter S_n, is to displace the minimum of the resistance towards cathodic potentials while for slower bulk recombination, tuned via the parameter B, this minimum is decreased and is associated to enhanced charge transfer kinetics.

In view of these simulations and the experimental results provided in **Figure 3f,** we can now identify the main recombination pathway for the three materials used in this

study. In **Figure 3f**, the minimum value of R_{dc} is obtained for the WO_3-$BiVO_4$ heterojunction, while the highest one corresponds to the WO_3 photoanode. We deduce that the lowest bulk recombination is found for the WO_3-$BiVO_4$ heterojunction while WO_3 suffers from the highest bulk recombination. In addition, the most cathodic voltage corresponding to the minimum of the charge transfer resistance is found for WO_3 and the most anodic voltage is obtained for $BiVO_4$, while an intermediate value is reached for WO_3-$BiVO_4$. We infer from such observations that electron extraction at the electron selective contact is faster for WO_3, compared to WO_3-$BiVO_4$, and is the slowest one for $BiVO_4$. In fact, for the WO_3-$BiVO_4$ heterostructure, the electron selective contact is in contact with both, WO_3 and $BiVO_4$ nanoparticles. For this reason, electron extraction from the WO_3-$BiVO_4$ electrode is faster than for pure $BiVO_4$ but slower than for pure WO_3.

The summary of our combined EIS analysis and modeling is depicted in **Figure 6**, which relates the microscopic physico-chemical processes occurring in each type of sample to the measured and simulated photo-electrochemical behavior of these devices. From this study, we deduce that the better performance obtained for the case of the WO_3-$BiVO_4$ heterojunction with respect to pure WO_3 and $BiVO_4$ samples is due to the injection of photogenerated carriers from $BiVO_4$ to WO_3 and the subsequent reduction of bulk recombination rather than enhanced carrier extraction at the electron selective contact.

Finally, according to the previous discussion, the effect of S_n and S_p on photo-electrochemical performance for water oxidation cannot a priori be distinguished. Therefore, enhancement of charge extraction at the electron selective contact or hole selective contact (electrolyte) should both produce the effect observed in **Figure 5b**

(black and red curve): a horizontal displacement of the dc resistance valley. In **Figure S5**, we show the comparison between the measured R_{dc} for the WO_3-$BiVO_4$ sample with and without hole scavenger. As expected, enhanced hole extraction produces a displacement of the R_{dc} valley to more cathodic bias, without changing the actual value of R_{dc}. Such result therefore confirms the predictions of our simulations.

Conclusions

Our results clearly indicate that WO_3 controls both the capacitive and transport properties of the heterostructured WO_3-$BiVO_4$ system, leading to enhanced charge extraction at the electron contact. Consequently, the enhanced light harvesting properties of $BiVO_4$ are synergistically coupled to the electronic properties of WO_3 as derived from both dynamic characterization and physical modeling. In particular, thanks to the simple model we have developed here, we could attribute the better photo-electrochemical performances of the WO_3-$BiVO_4$ heterojunction to a significant reduction of the bulk recombination with respect to WO_3 and $BiVO_4$. The conclusions of this study can be also extrapolated to different device architectures, integrating one-dimensional and more complex structures, as well as the heterostructures which consist of other varieties of components.

Acknowledgements

We thank financial support from University Jaume I through the project P11B2014-51, from Generalitat Valenciana (ISIC/ 2012/008 Institute of Nanotechnologies for Clean Energies and ACOMP/2015/105) and from the European Commission through the Seventh Framework Program [FP7/2007–2013] grant agreement 316494. The Serveis

Centrals at UJI (SCIC) are also acknowledged.

Additionalinformation

Electronic Supplementary Information (ESI) available:

† Both authors have equally contributed to this study

References

1. B. A. Pinaud, J. D. Benck, L. C. Seitz, A. J. Forman, Z. Chen, T. G. Deutsch, B. D. James, K. N. Baum, G. N. Baum, S. Ardo, H. Wang, E. Miller and T. F. Jaramillo, *Energy & Environmental Science*, 2013, **6**, 1983-2002.

2. A. Fujishima and K. Honda, *Nature*, 1972, **238**, 37-+.

3. A. Wolcott, W. A. Smith, T. R. Kuykendall, Y. Zhao and J. Z. Zhang, *Advanced Functional Materials*, 2009, **19**, 1849-1856.

4. M. A. Butler, *Journal of Applied Physics*, 1977, **48**, 1914-1920.

5. A. Kudo, K. Omori and H. Kato, *Journal of the American Chemical Society*, 1999, **121**, 11459-11467.

6. K. Sivula, F. Le Formal and M. Graetzel, *Chemsuschem*, 2011, **4**, 432-449.

7. X. Ma, Y. Dai and B. Huang, *Acs Applied Materials & Interfaces*, 2014, **6**, 22815-22822.

8. X. Ma, Y. Dai, L. Yu and B. Huang, *Nanoscale*, 2016, **8**, 1352-1359.

9. J. Y. Kim, G. Magesh, D. H. Youn, J.-W. Jang, J. Kubota, K. Domen and J. S. Lee, *Scientific Reports*, 2013, **3**.

10. S. C. Warren, K. Voitchovsky, H. Dotan, C. M. Leroy, M. Cornuz, F. Stellacci, C. Hebert, A. Rothschild and M. Graetzel, *Nature Materials*, 2013, **12**, 842-849.

11. J.-W. Jang, C. Du, Y. Ye, Y. Lin, X. Yao, J. Thorne, E. Liu, G. McMahon, J. Zhu, A. Javey, J. Guo and D. Wang, *Nature Communications*, 2015, **6**.

12. T. W. Kim and K.-S. Choi, *Science*, 2014, **343**, 990-994.

13. F. F. Abdi, L. Han, A. H. M. Smets, M. Zeman, B. Dam and R. van de Krol, *Nature Communications*, 2013, **4**.

14. P. Chatchai, Y. Murakami, S.-y. Kishioka, A. Y. Nosaka and Y. Nosaka, *Electrochimica Acta*, 2009, **54**, 1147-1152.

15. S. J. Hong, S. Lee, J. S. Jang and J. S. Lee, *Energy & Environmental Science*, 2011, **4**, 1781-1787.

16. P. M. Rao, L. Cai, C. Liu, I. S. Cho, C. H. Lee, J. M. Weisse, P. Yang and X.

Zheng, *Nano Letters*, 2014, **14**, 1099-1105.

17. J. Su, L. Guo, N. Bao and C. A. Grimes, *Nano Letters*, 2011, **11**, 1928-1933.

18. X. Shi, K. Zhang, K. Shin, M. Ma, J. Kwon, I. T. Choi, J. K. Kim, H. KyuKim, D. H. Wang and J. Hyeok Park, *Nano Energy*, 2015, **dx.doi.org/10.1016/j.nanoen.2015.02.018**.

19. Y. Pihosh, I. Turkevych, K. Mawatari, J. Uemura, Y. Kazoe, S. Kosar, K. Makita, T. Sugaya, T. Matsui, D. Fujita, M. Tosa, M. Kondo and T. Kitamori, *Scientific Reports*, 2015, **5**.

20. X. Shi, Y. Choi, K. Zhang, J. Kwon, D. Y. Kim, J. K. Lee, S. H. Oh, J. K. Kim and J. H. Park, *Nature Communications*, 2014, **5**.

21. M. G. Walter, E. L. Warren, J. R. McKone, S. W. Boettcher, Q. Mi, E. A. Santori and N. S. Lewis, *Chemical Reviews*, 2010, **110**, 6446-6473.

22. H. Dotan, K. Sivula, M. Graetzel, A. Rothschild and S. C. Warren, *Energy & Environmental Science*, 2011, **4**, 958-964.

23. J. Bisquert, G. Garcia-Belmonte, F. Fabregat-Santiago, N. S. Ferriols, P. Bogdanoff and E. C. Pereira, *The Journal of Physical Chemistry B*, 2000, **104**, 2287-2298.

24. J. Bisquert, *Journal of Physical Chemistry B*, 2002, **106**, 325-333.

25. L. Bertoluzzi, P. Lopez-Varo, J. A. Jimenez Tejada and J. Bisquert, *Journal of Materials Chemistry A*, 2016, DOI: 10.1039/c5ta03210e.

26. L. H. Mascaro, A. Pockett, J. M. Mitchels, L. M. Peter, P. J. Cameron, V. Celorrio, D. J. Fermin, J. S. Sagu, K. G. U. Wijayantha, G. Kociok-Koehn and F. Marken, *Journal of Solid State Electrochemistry*, 2015, **19**, 31-35.

27. D.-D. Qin, T. Wang, Y.-M. Song and C.-L. Tao, *Dalton Transactions*, 2014, **43**, 7691-7694.

28. S. Gimenez, H. K. Dunn, P. Rodenas, F. Fabregat-Santiago, S. G. Miralles, E. M. Barea, R. Trevisan, A. Guerrero and J. Bisquert, *Journal of Electroanalytical Chemistry*, 2012, **668**, 119-125.

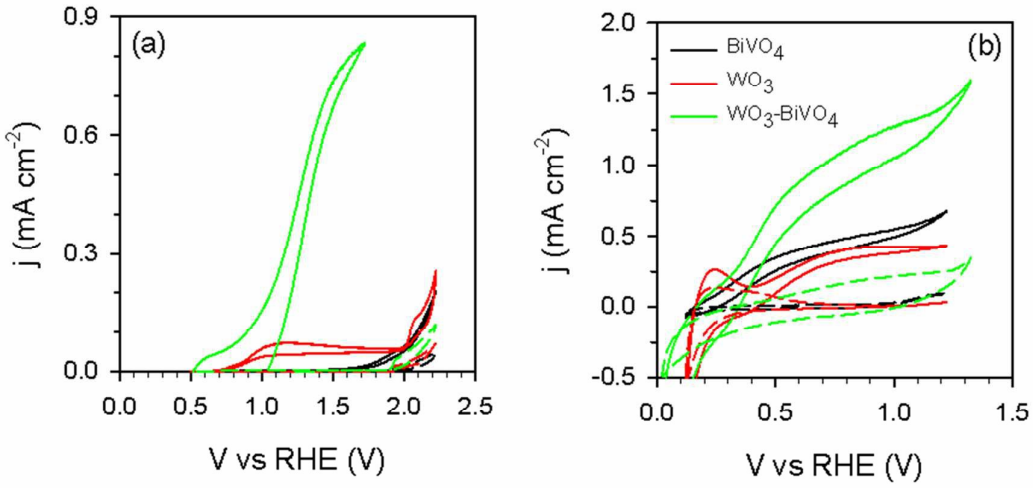

Figure 1. *j-V* curves of the different structures, WO_3, $BiVO_4$ and WO_3-$BiVO_4$ in the dark (dashed lines) and under illumination at 100 mW·cm^{-2} (solid lines), showing the synergistic effect of WO_3-$BiVO_4$ heterojunction system, (a) in a 0.5 M Na_2SO_4 solution at pH 7 and (b) same electrolyte with the presence of a hole scavenger (0.35 M Na_2SO_3)

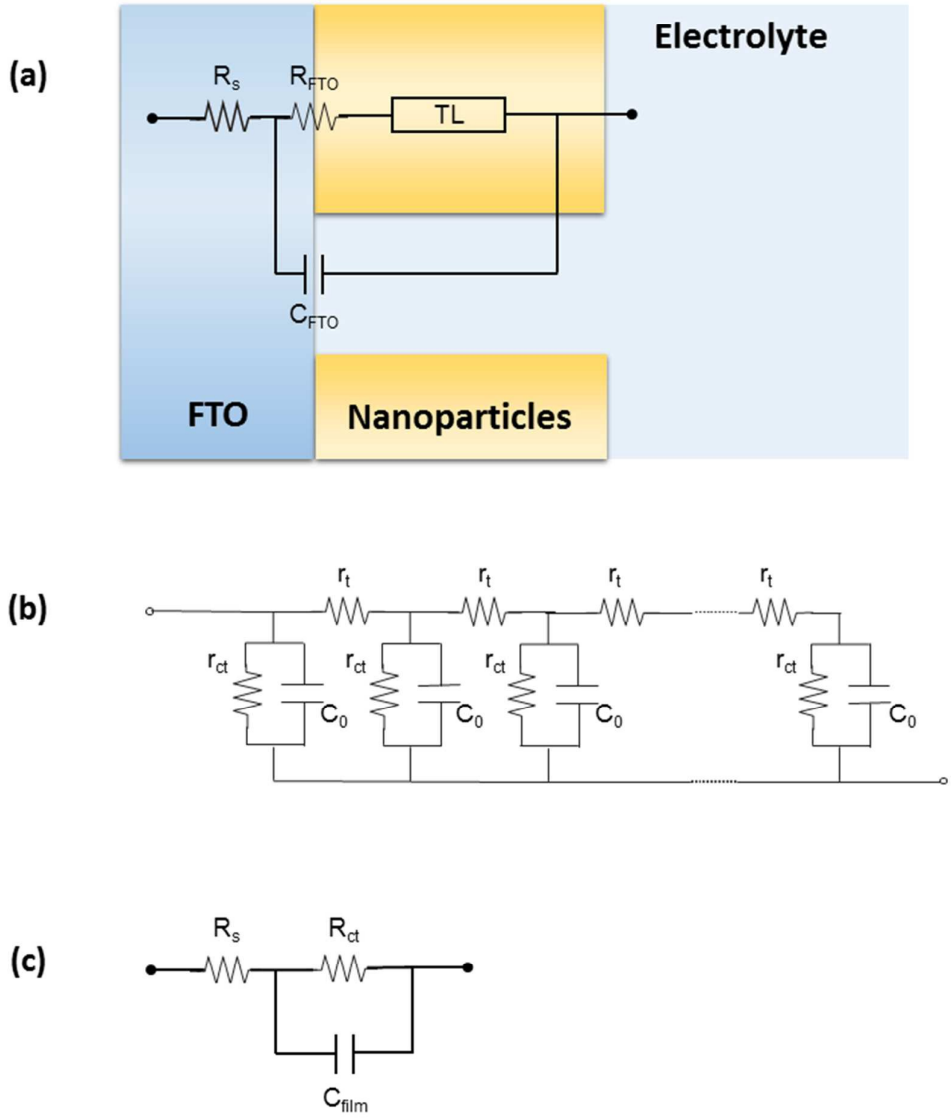

Figure 2.Equivalent circuit employed to fit the impedance spectra obtained in the dark and under illumination of (a) WO_3 containing samples, and (c) $BiVO_4$ samples. (b) Description of the transmission line element (TL). Transport resistance (R_t, or r_t), capacitance of the film (C_{film}, or C_0) and charge transfer resistance (R_{ct}, or r_{ct}).

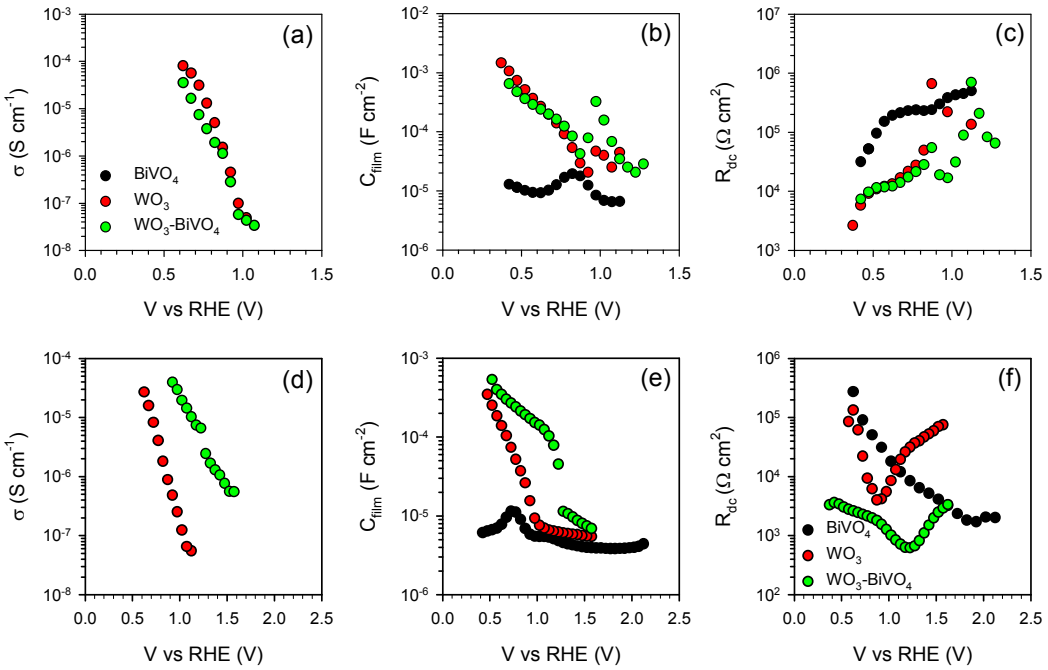

Figure 3.Parameters extracted from fitting the impedance spectra obtained in the dark (a, b and c) and under illumination (d, e and f) to the equivalent circuits showed in Figure 2. Conductivity (σ), Capacitance of the film (C_{film}) and dc resistance (R_{dc}).

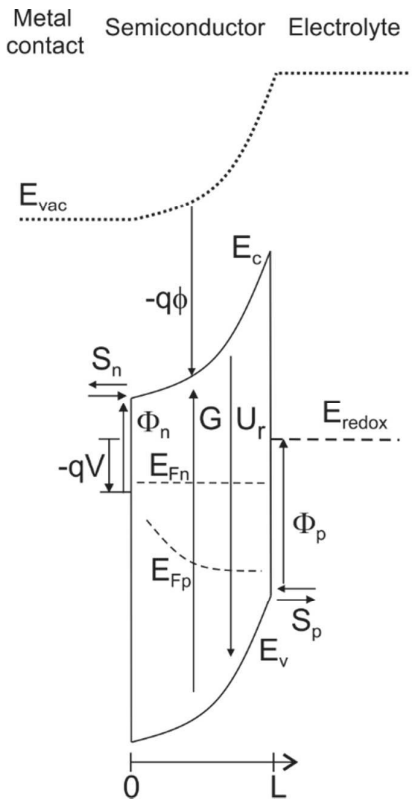

Figure 4. Band diagram of the metal/semiconductor/electrolyte junction for solar fuel applications including the rate of electron/hole pair generation, G, the kinetics of recombination of free carriers in the bulk (U_r) and at the surface (kinetic constants S_n for electrons and S_p for holes). In this representation E_c and E_v are the lower edge of the conduction band and the higher edge of the valence band, respectively, E_{Fn} and E_{Fp} are the quasi-Fermi level of electrons and holes, Φ_n and Φ_p are the injection barriers for electrons and holes respectively, E_{redox} is the energy level of the electrolyte, E_{vac} is the local vacuum level, ϕ is the local electrostatic potential and V is the applied potential which is referred to the redox level E_{redox}.

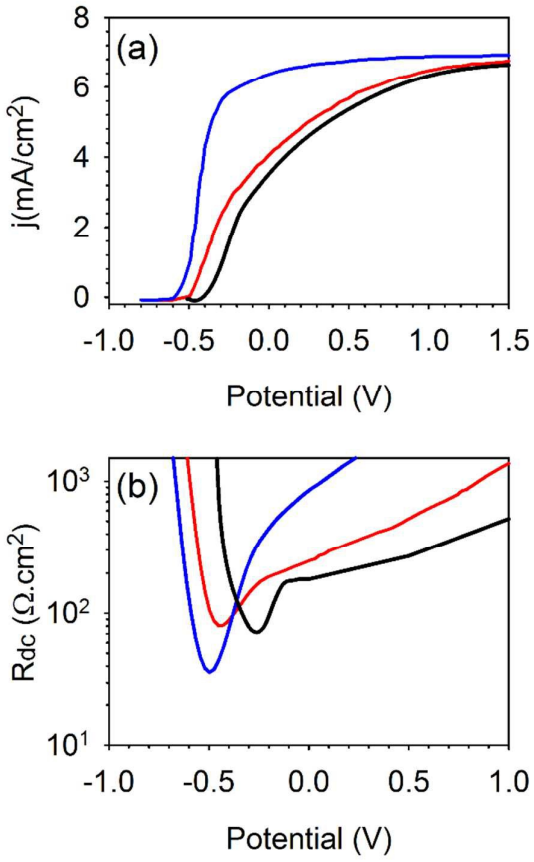

Figure 5. (a) *j-V* curves and (b) dc resistance for different values of the bulk recombination (B) and surface recombination at the electron selective contact (S_n). The values of the recombination rates are $B = 10^{-8}$ cm^3/s and $S_n = 10^{-2}$ cm/s (blue line), $B = 10^{-7}$ cm^3/s and $S_n = 10^{-2}$ cm/s (red line) and $B = 10^{-7}$ cm^3/s and $S_n = 10^{-4}$ cm/s (black line). The values of the other parameters used in our simulations are indicated in Table S2.

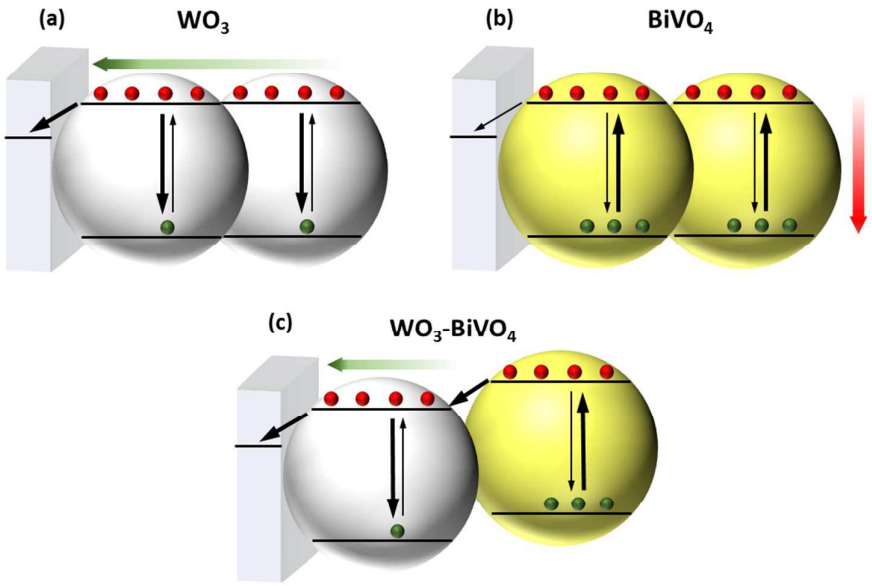

Figure 6. Scheme of the electronic processes (charge generation and recombination, electronic transport, and electron transfer at the electron selective contact) as deduced from our EIS analysis in the case of (a) pure WO_3, (b) pure $BiVO_4$, and (c) the WO_3-$BiVO_4$ heterojunction.

Understanding the synergistic effect of WO_3-$BiVO_4$ heterostructures by impedance spectroscopy

Graphical abstract

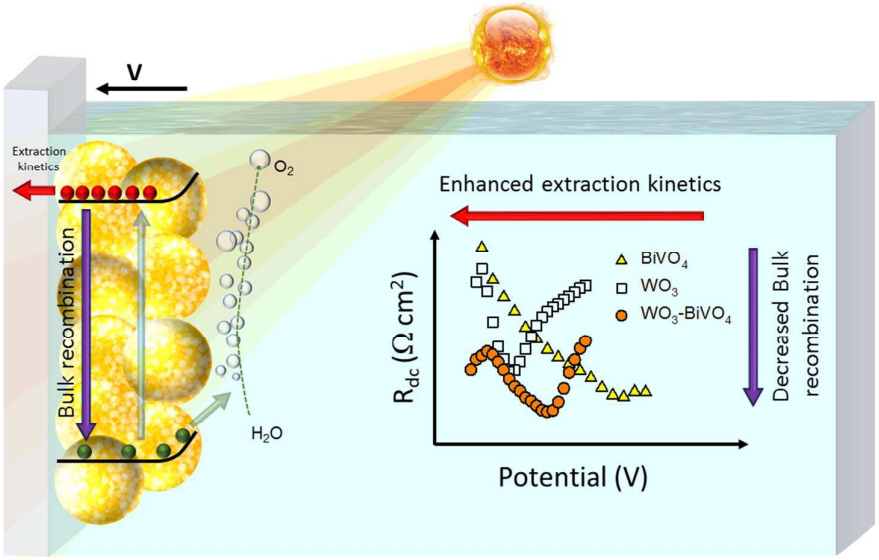

Scheme The dc resistance allows assessing the influence of bulk recombination and charge transfer kinetics on the oxygen evolution performed by heterostructured materials.